

OffsetNet: Deep Learning for Localization in the Lung using Rendered Images

Jake Sganga^{1*}, David Eng^{2*}, Chauncey Graetzel³ and David Camarillo¹

Abstract—Navigating surgical tools in the dynamic and tortuous anatomy of the lung’s airways requires accurate, real-time localization of the tools with respect to the preoperative scan of the anatomy. Such localization can inform human operators or enable closed-loop control by autonomous agents, which would require accuracy not yet reported in the literature. In this paper, we introduce a deep learning architecture, called OffsetNet, to accurately localize a bronchoscope in the lung in real-time. After training on only 30 minutes of recorded camera images in conserved regions of a lung phantom, OffsetNet tracks the bronchoscope’s motion on a held-out recording through these same regions at an update rate of 47 Hz and an average position error of 1.4 mm. Because this model performs poorly in less conserved regions, we augment the training dataset with simulated images from these regions. To bridge the gap between camera and simulated domains, we implement domain randomization and a generative adversarial network (GAN). After training on simulated images, OffsetNet tracks the bronchoscope’s motion in less conserved regions at an average position error of 2.4 mm, which meets conservative thresholds required for successful tracking.

I. INTRODUCTION

Early diagnosis of lung cancer, the leading cause of cancer death, significantly improves patient outcomes [1]. While nodules in the lung’s periphery can be diagnosed through thoroscopic surgery or needle biopsy, bronchoscopies are the preferred approach given the lower complication rates (2.2% vs 20.5%) [2], [3]. In bronchoscopy procedures, physicians manually drive long, flexible bronchoscopes through the patient’s airways to biopsy potentially cancerous nodules, shown in Fig. 1. Physicians rely on sensor feedback from an on-board camera and, in navigated bronchoscopy procedures, an electromagnetic position sensor at the distal tip of the device. The position sensor is registered to a preoperative computed tomography (CT) of the patient’s chest to provide a road map to the target site [4]. However, there is significant variability in the diagnostic yield among institutions ranging from 67-74% [2], [5]. Accurate localization and robotic control of bronchoscopes can alleviate this variability and improve patient outcomes.

Since the physician identifies target nodules in the CT reference frame before the operation begins, the physician must map the sensor feedback from the device (2D image) to

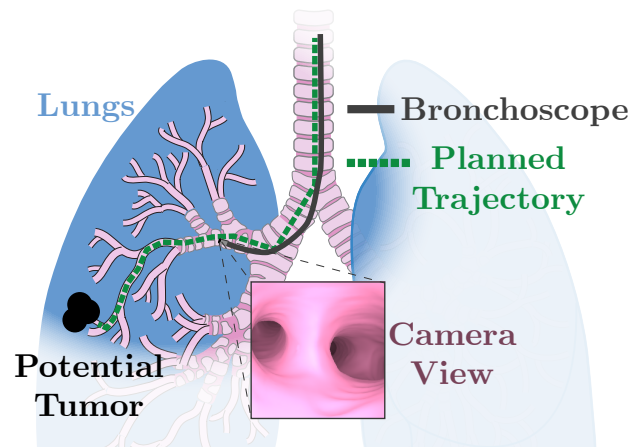


Fig. 1: The objective of a bronchoscopy is to navigate the bronchoscope to the site of a potential tumor given the trajectory from the preoperative CT scan. To do this, the operator must use the 2D images from the bronchoscope to determine where it is along the 3D path to the target.

the CT frame (3D map). This process is called localization. A localization module must inform the physician how the bronchoscope’s current location relates to its desired location. An autonomous agent could use this same information to “drive” the bronchoscope without human intervention.

We set out to design an image-based system that can localize in real-time and accurately enough to be used for closed-loop control in a robotic system. We consider image-based approaches instead of hybrid approaches that integrate information from electromagnetic position sensors because these sensors experience unknown biological motion of the patient, have the potential for noise and distortion from metal in the operating room, and increase the total cost of the system [6].

Using traditional computer vision techniques to solve this task accurately and in real-time has proven challenging. Several groups have compared the images from the bronchoscope to simulated images rendered from the estimated location of the bronchoscope in CT frame; however, these methods register images inefficiently at around 1-2 Hz with high average registration errors of 3-5 mm [7], [8], [6]. Tracking features using methods like SIFT and ORBSLAM have been used, but the airways have insufficient features and tracked features often drop out [9], [10]. Anatomical landmarks have been tracked, like bifurcations [11], lumen centers [12], centerline paths [13], or similar image regions [14], but these approaches make assumptions about the airway geometries and struggle with image artifacts.

*These authors contributed equally.

This work was supported by the NIH Biotechnology Training Grant, NVIDIA GPU Grant, and Auris Health, Inc.

¹Department of Bioengineering, Stanford University, Stanford, CA 94305

²Department of Computer Science, Stanford University, Stanford, CA 94305

³Auris Health Inc., Redwood City, CA 94065

{sganga,dkeng,dcamarillo}@stanford.edu
chauncey.graetzel@aurishealth.com

Merritt *et al.* describes a real-time localization approach with average errors as low as 1.4 mm in simulation [15]. Their method precomputes image gradients of simulated reference images along the anticipated procedure path and uses an iterative Gauss-Newton gradient-descent to determine the transformation between each camera image and the closest of these reference images. While this technique reports continuous tracking, it relies on high-quality rendering and a dense collection of reference images.

Because of the difficulties traditional computer vision techniques face in this task, we decided to explore a deep learning approach. Using convolutional neural networks (CNN) to estimate the position and orientation of objects has been shown in many contexts, including for human posture and objects in a hand [16], [17]. Visentini-Scarzanella *et al.* used a CNN to estimate the depth map of 2D images in a lung phantom, which could then be registered to the 3D map, but tracking is not reported [10].

In this work, we contribute an image-based deep-learning approach, called OffsetNet, that localizes a bronchoscope in the CT frame accurately and in real-time. We evaluate OffsetNet on a recorded trajectory in a lung phantom, demonstrating continuous, real-time tracking. We also show that training on simulated images can improve the performance in regions of the lung without recorded training data. To the authors' knowledge, this is the first deep-learning approach for localizing a bronchoscope.

TABLE I: Notation

| Input Images into OffsetNet (Fig. 2) | |
|--|--|
| \mathbf{I}_x^{sty} | Generically, an image with style sty at 6-DOF location, x |
| \mathbf{I}_{x_t} | Image from the bronchoscope's current location, x_t |
| $\mathbf{I}_{\hat{x}_{t-1}}$ | Image rendered at the previously estimated location, \hat{x}_{t-1} |
| Image Styles (Fig. 5) | |
| \mathbf{I}^{cam} | Image taken by a bronchoscope in the lung phantom |
| \mathbf{I}^{sim} | Image rendered by OpenGL using the lung CT |
| \mathbf{I}^{rsim} | Image rendered by OpenGL using the lung CT with varied rendering parameters and varied noise, smoothing and occlusions added [18] |
| \mathbf{I}^{gsim} | Image rendered by OpenGL using the lung CT, then passed through the generator of a trained GAN (generative adversarial network) [19] |
| Error between True and Estimated Locations | |
| e_p | Position error (mm), defined as e_p in [15] |
| e_d | Direction angle error between pointing vectors, p_z , of the two views ($^\circ$), defined as e_d in [15] |
| e_r | Roll angle error between the p_x axis after the e_d was corrected for between views ($^\circ$), defined as e_r in [15] |
| $\ \cdot\ _E$ | Location error, $e_p + 0.175e_d + 0.175e_r$, (mm, $^\circ$) |
| Lung Regions (Fig. 6) | |
| C | Airways in the lung where \mathbf{I}^{cam} images were included in the training set, representing conserved regions among patients |
| U | Airways in the lung where \mathbf{I}^{cam} images were omitted from the training set, representing less conserved regions |

II. METHOD

In this approach, we compare \mathbf{I}_{x_t} , the image from the bronchoscope's current location x_t , to $\mathbf{I}_{\hat{x}_{t-1}}$, the image rendered at the bronchoscope's estimated location from the previous timestep \hat{x}_{t-1} , shown in Fig. 2, and estimate the location offset between the images, $\Delta\hat{x}$. This offset updates the estimated bronchoscope location for the current timestep according to $\hat{x}_t \leftarrow \hat{x}_{t-1} + \Delta\hat{x}$, which is used to render the image at the bronchoscope's estimated location in the next

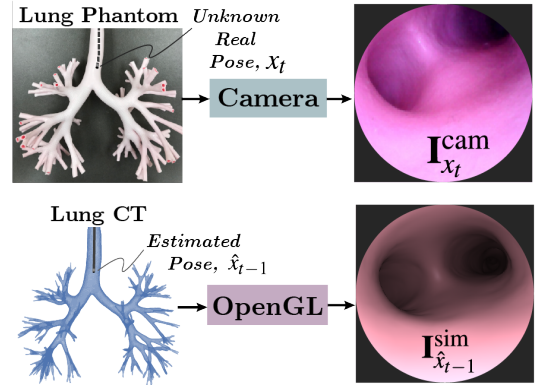


Fig. 2: The input to OffsetNet is a $(\mathbf{I}_{x_t}^{cam}, \mathbf{I}_{\hat{x}_{t-1}}^{sim})$ image pair, shown here. A bronchoscope inside the lung generates $\mathbf{I}_{x_t}^{cam}$, and a rendering of the estimated pose in the lung's CT model creates $\mathbf{I}_{\hat{x}_{t-1}}^{sim}$. The task is to identify the offset between them, and through repeated iterations, reduce the offset as much as possible.

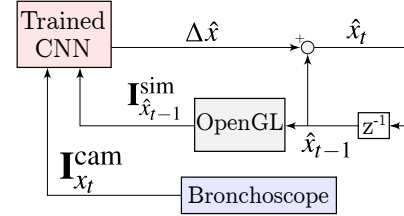


Fig. 3: This control loop describes the tracking task, where a trained CNN (OffsetNet) receives a $(\mathbf{I}_{x_t}^{cam}, \mathbf{I}_{\hat{x}_{t-1}}^{sim})$ image pair at time t and outputs the estimated 6-DOF offset, $\Delta\hat{x}$. The estimated location \hat{x}_t is updated, and the updated location is used to render the next $\mathbf{I}_{\hat{x}_t}^{sim}$.

time step. By iteratively updating the estimated location, the algorithm can track the motion of the bronchoscope, shown in Fig. 3.

Our system consists of two independent deep residual convolutional networks (CNN) with identical architectures, shown in Fig. 4. For each $(\mathbf{I}_{x_t}, \mathbf{I}_{\hat{x}_{t-1}})$ image pair, we feed \mathbf{I}_{x_t} into the first network and $\mathbf{I}_{\hat{x}_{t-1}}$ into the second network, concatenate the embeddings, and pass the resulting vector through a fully-connected layer, which produces an estimate of the pose of the first image in the frame of the second image. This length 6 vector, $\Delta\hat{x}$, consists of 3 components describing the position offset $\Delta\hat{x}_p = [p_x, p_y, p_z]$ (mm) and 3 components describing the rotation offset $\Delta\hat{x}_r = [\alpha, \beta, \gamma]$ ($^\circ$), defined by the three Euler angles about axes xyz [20]. We define positive p_z into the page, and positive p_x to the right.

The residual parts of our network implement the 34-layer architecture described in He *et al.* [21]. The CNN was implemented in Tensorflow, version 1.9 [22].

The network is trained using Adam optimization ($\beta_1 = 0.9$, $\beta_2 = 0.999$, $\epsilon = 10^{-8}$) to minimize a weighted L2 loss function $\ell(\Delta\hat{x}, \Delta x)$ between the estimated offset, $\Delta\hat{x}$, and the ground-truth offset, Δx . To relate position and rotation errors, we chose a 1 mm:5.7 $^\circ$ ratio, which roughly relates to the fact that a 5.7 $^\circ$ e_d angle error results in an error of 1 mm for a

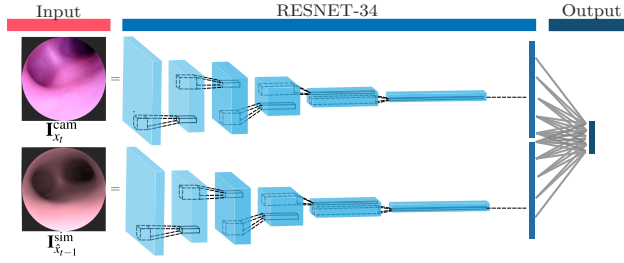


Fig. 4: OffsetNet architecture overview show two Resnet-34's processing each image input, followed by a fully connected later, and outputting a 6D vector representing a translation (mm) and rotation (°) [21].

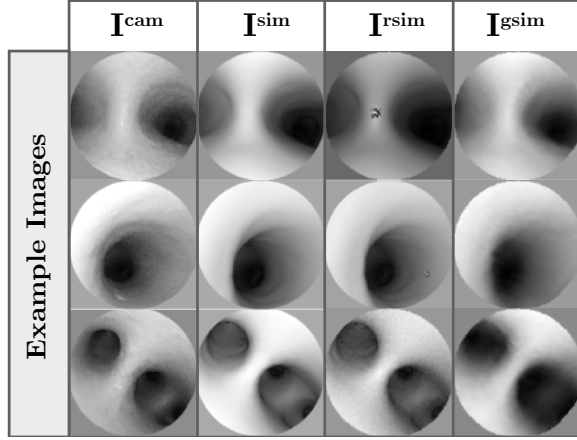


Fig. 5: Example images of the lung airways based on image style after grayscaling, adding a circle mask, and per-image normalizing to zero mean and unit standard deviation.

location 10 mm in front of the camera:

$$\ell(\Delta\hat{x}, \Delta x) = \|\Delta\hat{x}_p - \Delta x_p\|_2^2 + (1/5.7) \cdot \|\Delta\hat{x}_r - \Delta x_r\|_2^2$$

When deployed, our control loop compares $\mathbf{I}_{x_t}^{\text{cam}}$, captured by the bronchoscope's camera from its current location, and $\mathbf{I}_{\hat{x}_{t-1}}^{\text{sim}}$, rendered at the bronchoscope's previous estimated location. To reflect this, we evaluate our models on test sets consisting of $(\mathbf{I}_{x_t}^{\text{cam}}, \mathbf{I}_{\hat{x}_{t-1}}^{\text{sim}})$ image pairs. We train our models on training sets consisting of $(\mathbf{I}_{x_t}^{\{\text{cam}, \text{sim}, \text{rsim}, \text{gsim}\}}, \mathbf{I}_{\hat{x}_{t-1}}^{\text{sim}})$ image pairs, where the style of the image from the bronchoscope's current location varies according to the experiment. Note that all image pairs consist of $(\cdot, \mathbf{I}_{\hat{x}_{t-1}}^{\text{sim}})$.

All \mathbf{I}^{cam} images were created by manually driving a robotic bronchoscope (Monarch Platform, Auris Health Inc.) for 30 minutes in a lung phantom (Koken Co.), covering 3-5 generations of both lungs. For the experiments presented, OffsetNet was trained on data in the left lung to reduce the data file sizes, shown in Fig 6. While driving, a 6-DOF electromagnetic sensor (Northern Digital Inc.) tracked the bronchoscope and provided an initial, coarse estimate of the location in CT frame \hat{x}_t from which each $\mathbf{I}_{x_t}^{\text{cam}}$ was captured. However, a single rigid registration of the sensor's output resulted in errors of up to several millimeters, so local registrations were iteratively refined to improve the label quality. Local registrations were performed by manually translating and rotating nearby points (within a 2 cm cube) until the pixel-wise error $\|\mathbf{I}_{x_t}^{\text{sim}} - \mathbf{I}_{x_t}^{\text{cam}}\|_2$ reached a local

minimum. Powell's method was used in conjunction with manual optimization to refine \hat{x}_t to a ground-truth location in CT frame x_t [23].

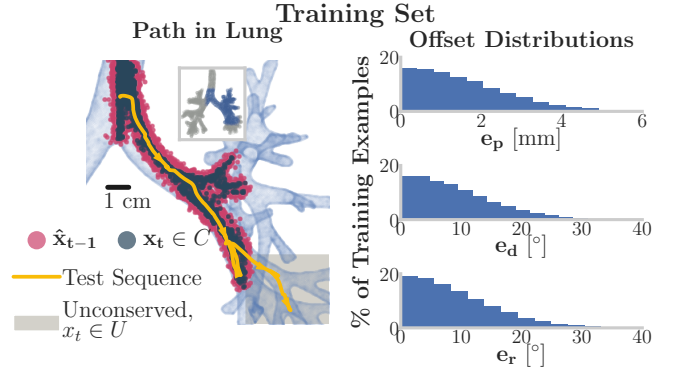


Fig. 6: Left, a sample of the 24958 locations $x_t \in C$ and \hat{x}_{t-1} used in the training set. The 750 locations of the test sequence are highlighted. Notice the unconserved region lacks any x_t . Right, the distributions of offsets between the (x_t, \hat{x}_{t-1}) pairs is shown for e_p , e_d and e_r .

All \mathbf{I}^{sim} images are rendered using PyOpenGL [24] and a 3D lung STL from a segmented CT scan of the lung phantom (Monarch Platform, Auris Health Inc.) [25]. The rendering parameters are based on Higgins *et al.* with a field of view of 60° [26]. Images are rendered at 60 Hz on a PC with no accelerations. The lighting and color were optimized to reduce the pixel-wise difference between images with different styles at the same location, $\mathbf{I}_{x \in C}^{\text{sim}}$ and $\mathbf{I}_{x \in C}^{\text{cam}}$, after grayscaling and per-image normalization. The quality of the segmentation critically affects the quality of \mathbf{I}^{sim} .

Training sets used in Section III-B also consist of \mathbf{I}^{rsim} and \mathbf{I}^{gsim} images. Tobin *et al.* first introduced \mathbf{I}^{rsim} images, which were rendered with randomized parameters to generalize their CNN across these changes [18]. We randomized each parameter with a normal distribution centered about the default rendering parameters. For these experiments, brightness, attenuation factor, specular intensity, and ambient intensity were all varied by 1, 0.001, 0.1, and 0.1, respectively. In addition, we used randomized Gaussian smoothing, and on half of the images, we added independent per-pixel noise and white noise occlusions of various sizes.

To make our rendered images more closely resemble \mathbf{I}^{cam} , we trained a GAN, following the general design principles described in Zhu *et al.* [19]. We adopted the architecture for our generative network from Johnson *et al.* [27]. For the discriminator networks, we used 14×14 PatchGANs. We encouraged a pixel-wise similarity between the transferred \mathbf{I}^{cam} and the actual \mathbf{I}^{cam} images, as well as the transferred \mathbf{I}^{sim} and the actual \mathbf{I}^{sim} images in our loss function. We trained on 1000 total $\mathbf{I}_{x \in C}^{\text{sim}}$ images and 1000 total $\mathbf{I}_{x \in C}^{\text{cam}}$ images. We replaced negative log-likelihood objective by a least-squares loss function, as in [19].

To generate datasets consisting of $(\mathbf{I}_{x_t}, \mathbf{I}_{\hat{x}_{t-1}})$ image pairs, we generate a $\mathbf{I}_{\hat{x}_{t-1}}$ at a location \hat{x}_{t-1} offset from the registered location x_t according to normal distributions of e_p , e_d , and e_r . The distributions used for the training had 0 mean and standard deviations of 2 mm, 11°, 11°, respectively,

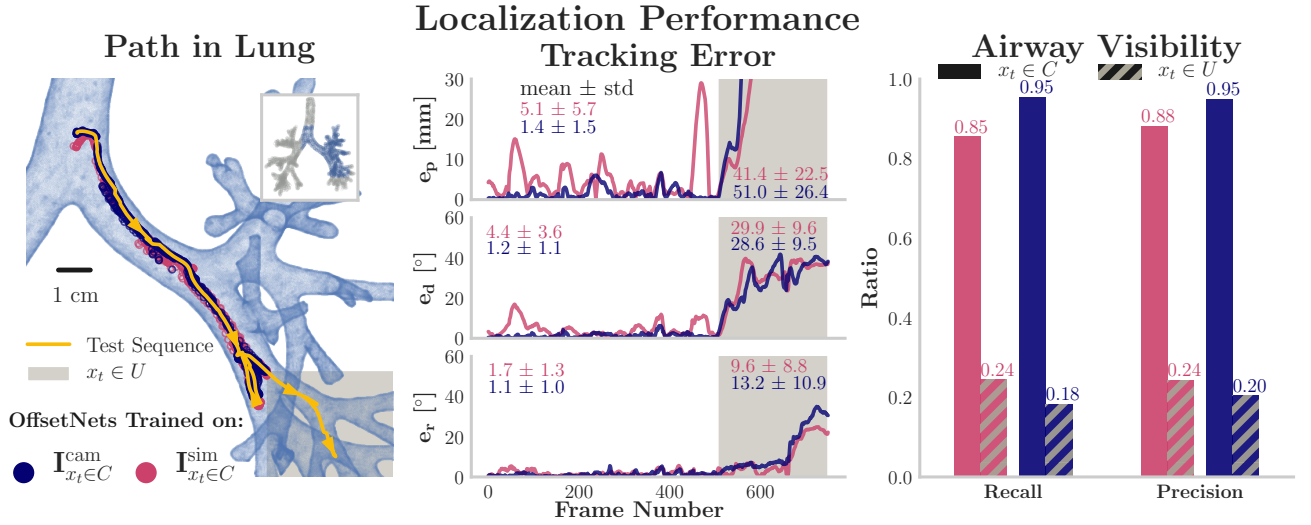


Fig. 7: Two OffsetNets are shown in a tracking task on the test sequence, $\mathbf{I}_x^{\text{cam}}$. Note that all models were trained on $(\cdot, \mathbf{I}_{\hat{x}_{t-1}}^{\text{sim}})$ image pairs. Left, the path and estimated positions are shown on the lung CT. Middle, the tracking error in e_p , e_d , and e_r are shown over the frame sequence, and the frames in the unconstrained region are highlighted in gray. Right, the airway visibility analysis shows recall and precision ratios for the conserved and unconstrained (hatched) regions.

shown in Fig. 6. Each $\mathbf{I}_{x_t}^{\text{cam}}$ was augmented by rotating the images with a 14° standard deviation.

Training sets in Section III-A comprised of 200 $(\mathbf{I}_{x_t}^{\text{cam}}, \mathbf{I}_{\hat{x}_{t-1}}^{\text{sim}})$ image pairs per original recorded location, x_t^{rec} . For every pair, x_t was offset from x_t^{rec} in roll only. Training sets in Section III-B comprised of 750 $(\mathbf{I}_{x_t}^{\{\text{sim}, \text{rsim}, \text{gsim}\}}, \mathbf{I}_{\hat{x}_{t-1}}^{\text{sim}})$ image pairs, at locations x_t offset from recorded locations x_t^{rec} in the test sequence. In all training sets, each location \hat{x}_{t-1} was offset from the resulting location x_t .

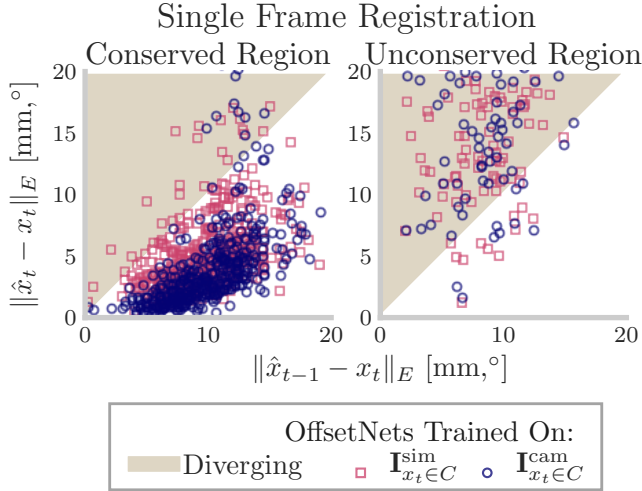


Fig. 8: OffsetNets tested on a dataset of $(\mathbf{I}_{x_t}^{\text{cam}}, \mathbf{I}_{\hat{x}_{t-1}}^{\text{sim}})$ image pairs along the full test sequence. 25 \hat{x}_{t-1} locations were randomly offset from each x_t . Note that all models were trained on $(\cdot, \mathbf{I}_{\hat{x}_{t-1}}^{\text{sim}})$ image pairs. Each axis is a linear combination of translation and rotation error, defined in Table I. Diverging estimates are defined by the $\|\hat{x}_t - x_t\|_E > \|\hat{x}_{t-1} - x_t\|_E$. One out of every 30 points are plotted for visibility, and results from the conserved and unconstrained region are plotted separately.

III. RESULTS

On a laptop PC with a 2.70 GHz CPU, the tracking loop ran at an average of 47.7 Hz, while the bronchoscope receives images at a rate of 25-30 Hz.

A. OffsetNet Tracks Test Sequence in Conserved Region

We trained OffsetNet on $(\mathbf{I}_{x_t \in C}^{\text{cam}}, \mathbf{I}_{\hat{x}_{t-1}}^{\text{sim}})$ image pairs from conserved regions in the left lung phantom, denoted the “conserved” region S . To study the contribution of image style, we also trained a model on $(\mathbf{I}_{x_t \in C}^{\text{sim}}, \mathbf{I}_{\hat{x}_{t-1}}^{\text{sim}})$ image pairs rendered in the same positions and orientations x_t . Both models were evaluated on a held-out test sequence that passed through the conserved regions of the lung phantom on which the model had been trained (conserved region) and through a less conserved region that had no training images (unconstrained region), shown in Fig. 6.

In Fig. 8, the models were analyzed in a single-frame registration task, where each \mathbf{I}_{x_t} of the test sequence was tested against 25 uniformly offset $\mathbf{I}_{\hat{x}_{t-1}}$ and the results are shown separately for the conserved and unconstrained regions of the lung. The $\mathbf{I}_{\hat{x}_{t-1}}$ were uniformly offset by 0-10 mm in e_p , 0-43° in e_d , 0-43° in e_r . This range covers beyond what the models were trained on to show their limits. Fig. 8 visualizes this result by combining translation (mm) and rotation (°) offsets into a single distance measure, defined in Table I, which mimics the training loss function. When the updated location error is greater than the initial location error, OffsetNet diverges from the location estimate. Because OffsetNet’s performance is correlated with the initial location error, diverging estimates increase the likelihood of failure. The results are reported in Table II as models $a-d$ for each dimension (e_p , e_d , e_r).

Fig. 7 shows OffsetNet tracking the test sequence of $\mathbf{I}_x^{\text{cam}}$, where the output of each step updated the estimated \hat{x}_t to be used in the following step as shown in Fig. 3. The model trained on $(\mathbf{I}_{x_t \in C}^{\text{cam}}, \mathbf{I}_{\hat{x}_{t-1}}^{\text{sim}})$ image pairs tracks the

TABLE II: Results of single-frame registration task on a dataset of $(\mathbf{I}_{x_t}^{\text{cam}}, \mathbf{I}_{\hat{x}_{t-1}}^{\text{sim}})$ image pairs along the test sequence. Errors reported as mean \pm standard deviation.

| Trained On Image Styles: | e_p [mm] | e_d [°] | e_r [°] | Converging Estimates |
|---|----------------|-----------------|-----------------|----------------------|
| <i>Trained in conserved region, Tested in conserved region</i> | | | | |
| <i>a</i> $(\mathbf{I}_{x_t \in C}^{\text{cam}}, \mathbf{I}_{\hat{x}_{t-1}}^{\text{sim}})$ | 2.9 ± 3.3 | 4.2 ± 6.6 | 4.3 ± 7.6 | 94% |
| <i>b</i> $(\mathbf{I}_{x_t \in C}^{\text{sim}}, \mathbf{I}_{\hat{x}_{t-1}}^{\text{sim}})$ | 3.7 ± 3.3 | 5.6 ± 6.2 | 4.4 ± 7.5 | 91% |
| <i>Trained in conserved region, Tested in unconserve region</i> | | | | |
| <i>c</i> $(\mathbf{I}_{x_t \in C}^{\text{cam}}, \mathbf{I}_{\hat{x}_{t-1}}^{\text{sim}})$ | 14.5 ± 9.3 | 20.5 ± 13.0 | 23.4 ± 15.4 | 9% |
| <i>d</i> $(\mathbf{I}_{x_t \in C}^{\text{sim}}, \mathbf{I}_{\hat{x}_{t-1}}^{\text{sim}})$ | 10.2 ± 5.9 | 20.6 ± 12.0 | 22.4 ± 15.0 | 11% |
| <i>Trained in all regions, Tested in unconserve region</i> | | | | |
| <i>e</i> $(\mathbf{I}_{x_t}^{\text{sim}}, \mathbf{I}_{\hat{x}_{t-1}}^{\text{sim}})$ | 3.8 ± 2.3 | 9.2 ± 7.6 | 6.2 ± 8.9 | 80% |
| <i>f</i> $(\mathbf{I}_{x_t}^{\text{rsim}}, \mathbf{I}_{\hat{x}_{t-1}}^{\text{sim}})$ | 3.2 ± 2.4 | 7.5 ± 7.7 | 6.0 ± 8.6 | 88% |
| <i>g</i> $(\mathbf{I}_{x_t}^{\text{gsim}}, \mathbf{I}_{\hat{x}_{t-1}}^{\text{sim}})$ | 3.6 ± 2.2 | 8.9 ± 7.9 | 7.2 ± 8.6 | 81% |

bronchoscope until the bronchoscope enters the unconserve region, at which point the estimate jitters around previously conserved bifurcations. The maximum error in the conserved region was 6.7 mm, 6.3° in e_d and 5.6° in e_r . The model trained on $(\mathbf{I}_{x_t \in C}^{\text{sim}}, \mathbf{I}_{\hat{x}_{t-1}}^{\text{sim}})$ image pairs also failed to track in the unconserve region, but surprisingly recovered from large errors in the conserved region. Its maximum errors in the conserved region were 29.0 mm, 16.9° in e_d and 5.7° in e_r .

To analyze how the tracking performances would relate to driving decisions, the visibility of airways at each location is analyzed. We define a visible airway as one whose centerline lies within 3 cm of the bronchoscope location and would lie within the location's field of view. Let a_t be the set of airways visible at x_t , and \hat{a}_t be the set of airways visible at the estimated location, \hat{x}_t . Recall is the true positive rate, $\sum a_t \cap \hat{a}_t / \sum \hat{a}_t$, while precision is the positive predictive value, $\sum a_t \cap \hat{a}_t / \sum a_t$. Low recall indicates OffsetNet missed visible airways, while low precision indicates OffsetNet misclassified airways as visible. The values reported are averaged over all t .

Along with low tracking errors, OffsetNet trained on $(\mathbf{I}_{x_t \in C}^{\text{cam}}, \mathbf{I}_{\hat{x}_{t-1}}^{\text{sim}})$ image pairs misclassified only 5% of airways as visible, resulting mainly from the point of maximum error when it pauses at a bifurcation before continuing to track. If an autonomous agent were commanded to follow the trajectory, it is possible it would steer towards one of these mislabeled airways, but the error rate is low enough that the performance may enable autonomous driving.

B. Training with Simulated Images Enables Tracking in Unconserve Region

In the lung periphery, the airway geometry is less conserved between patients, and the last section shows that OffsetNet's performance is extremely sensitive to unconserve airway geometry [28]. We explore if training on rendered image pairs in the conserved and unconserve regions, $(\mathbf{I}_{x_t}^{\{\text{sim}, \text{rsim}, \text{gsim}\}}, \mathbf{I}_{\hat{x}_{t-1}}^{\text{sim}})$, would enable patient-specific refinement to the model. For this experiment, models are tested on $\mathbf{I}_{x \in U}^{\text{cam}}$, the subset of the images from the test sequence that lies in the unconserve region U . Models were trained on image pairs where both (x_t, \hat{x}_{t-1}) were randomly offset around the recorded test sequence, x_t^{rec} , which generously targets the training around the test path. To evaluate the contribution of image style, models were

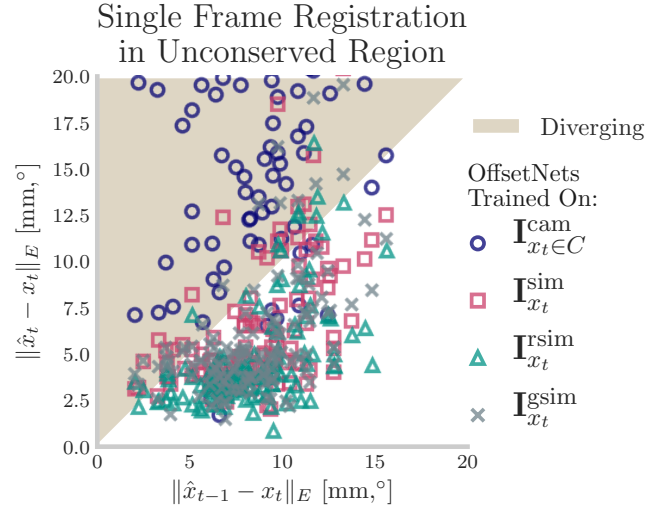


Fig. 9: OffsetNets tested on 25 uniformly offset $(\mathbf{I}_{x_t \in U}^{\text{cam}}, \mathbf{I}_{\hat{x}_{t-1}}^{\text{sim}})$ image pairs per x_t of the test sequence in the unconserve region of the lung, similar to Fig. 8. One out of every 50 points are plotted to improve visibility.

trained on $(\mathbf{I}_{x_t}^{\{\text{sim}, \text{rsim}, \text{gsim}\}}, \mathbf{I}_{\hat{x}_{t-1}}^{\text{sim}})$ image pairs, shown in Fig. 5. The three simulation-based models e, f, g were compared to model c trained on $(\mathbf{I}_{x_t \in C}^{\text{cam}}, \mathbf{I}_{\hat{x}_{t-1}}^{\text{sim}})$ image pairs.

They were tested on the single-frame registration task, shown in Fig. 9 and Table II. Models e, f, g trained on simulated data outperform model c on all metrics. Model f trained on $(\mathbf{I}_{x_t}^{\text{rsim}}, \mathbf{I}_{\hat{x}_{t-1}}^{\text{sim}})$ image pairs performs the best on each metric by a small margin. The differences in performance between models b and e can be attributed to differences in training distribution and task difficulty.

The models were also tested on a tracking task in the unconserve region, Fig. 10. In the tracking task, the model with no training in the region moves in the opposite direction, while all the simulation-based models track until at least the first bifurcation. Model f performs the best, successfully tracking the bronchoscope into the second airway after a maximum error of 13.0 mm, 18.6° in e_d , and 8.7° in e_r .

IV. DISCUSSION

The results of OffsetNet in a lung phantom demonstrate potential for being used as a real-time lung localization method. Based on only 30 minutes of training data, OffsetNet can track a held-out driving sequence in a lung phantom in real-time with accuracy comparable to or better than results reported in the literature, to the authors' knowledge. While the performance on the lung phantom may not be accurate enough to use in closed-loop control with an autonomous operator based on simulated training alone, we found that OffsetNet is capable of closing the loop in a simulated driving environment with sufficient training data; however, these results are not shown here due to space constraints.

Training on simulated data enabled tracking in a region of the lung phantom, which is an impressive result given the challenges in domain adaption for RGB cameras. This result is promising for handling airways unique to the patient in less conserved regions, given an accurate CT segmentation.

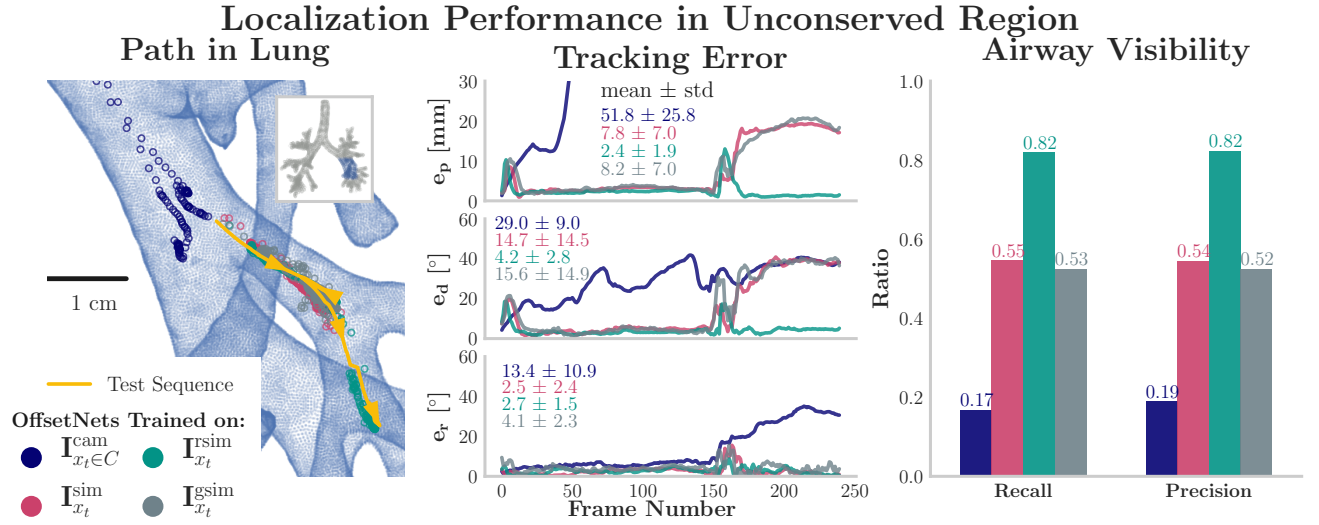


Fig. 10: Similar to Fig. 7, four OffsetNets are shown in a tracking task on a subset of the test sequence in the unconserved region. Left, the path and estimated positions are shown on the lung CT. Middle, the tracking error in e_p , e_d , and e_r are shown as functions of the video frame number. Right, the airway visibility analysis shows recall and precision.

While training on $(\mathbf{I}_{x_t}^{\text{sim}}, \mathbf{I}_{x_{t-1}}^{\text{sim}})$ image pairs performed better than $(\mathbf{I}_{x_t}^{\text{cam}}, \mathbf{I}_{x_{t-1}}^{\text{sim}})$ image pairs here, there is room to combine both methods, and refining the GAN performance would improve OffsetNet’s performance.

OffsetNet has the potential to incorporate more information by introducing additional $\mathbf{I}_{x_{t-1}}$ images into the tracking loop. For example, the predicted view from the centerline given the insertion information can help prevent the model from getting stuck. Multiple $\mathbf{I}_{x_{t-1}}$ images can also provide some insight into how much confidence the model has in its predictions by measuring the variance of the resulting estimates. To maintain real-time rates, the code can be optimized by moving from Python to C++.

The algorithm has several limitations, including geometry sensitivity and tracking unpredictability. OffsetNet fails to track in airways missing from its training set. Based on the model’s performance in the conserved and unconserved regions, it appears that OffsetNet fails to generalize to unconserved airways, which emphasizes the need for creating complete training sets. OffsetNet’s tracking performance is hard to predict as evidenced by the performance in Fig. 10 when model f can recover from an error, while the other models do not. More generally, stability is a risk for the tracking loop as it is only a matter of time before the location estimates \hat{x} drift (Fig. 3). In our tracking analysis, we strive to relate quantitative errors to the quality of the localization module, but it is imperfect. The definition of visible airways is somewhat arbitrary and may affect the reported results. In this paper, we only trained and tested OffsetNet on a limited dataset of a single lung phantom, which is considerably easier than the task of live human lungs. Finally, regardless of the algorithm, visual-based localization may struggle in the periphery of the lung when vision is lost because of airway collapse. Irrigation and air insufflation can help mitigate this issue, but there are times where the user needs to drive

without vision.

In conclusion, this technique shows promise as an accurate, real-time localization method in the lung’s airways. This same technique may be applied to other organ systems as well, given a suitable model of the geometry.

APPENDIX

OffsetNet is most similar to the inverse-compositional registration technique (IC), and the table below compares the reported values in a single-frame registration task to OffsetNet [15]. Note that the distribution of images differs from the single-frame registration tasks reported above.

TABLE III: Median errors for single-frame registration under random initial pose perturbations. The errors and success rate are defined in [15]. Results are shown for OffsetNet trained on $(\mathbf{I}_{x_t \in C}^{\text{cam}}, \mathbf{I}_{x_{t-1}}^{\text{sim}})$ image pairs [a] and $(\mathbf{I}_{x_t \in C}^{\text{sim}}, \mathbf{I}_{x_{t-1}}^{\text{sim}})$ image pairs [b], defined in Table II, evaluated in the conserved region.

| (a) Tested on $(\mathbf{I}_{x_t \in C}^{\text{sim}}, \mathbf{I}_{x_{t-1}}^{\text{sim}})$ image pairs | | | | |
|--|--------|-------|-------|--------------|
| Method | e_p | e_d | e_r | Success rate |
| IC [15] | 1.6 mm | 3.1° | 1.7° | 84% |
| OffsetNet [a] | 2.4 mm | 3.4° | 2.0° | 90.2% |
| OffsetNet [b] | 1.1 mm | 1.2° | 0.9° | 99.4% |

| (b) Tested on $(\mathbf{I}_{x_t \in C}^{\text{cam}}, \mathbf{I}_{x_{t-1}}^{\text{sim}})$ image pairs | | | | |
|--|--------|-------|-------|--------------|
| Method | e_p | e_d | e_r | Success rate |
| IC [15] | 2.7 mm | 5.4° | 8.2° | 70% |
| OffsetNet [a] | 1.2 mm | 1.2° | 1.1° | 99.3% |
| OffsetNet [b] | 2.0 mm | 3.1° | 1.4° | 91.0% |

ACKNOWLEDGMENT

We’d like thank Auris Health Inc. for the equipment and support, NVIDIA for the Titan X GPU.

REFERENCES

- [1] C. S. Dela Cruz, L. T. Tanoue, and R. A. Matthay, "Lung cancer: epidemiology, etiology, and prevention." *Clinics in chest medicine*, vol. 32, no. 4, pp. 605–44, dec 2011.
- [2] D. E. Ost, *et al.*, "Diagnostic Yield and Complications of Bronchoscopy for Peripheral Lung Lesions. Results of the AQUIRE Registry," *American Journal of Respiratory and Critical Care Medicine*, vol. 193, no. 1, pp. 68–77, jan 2016.
- [3] D. M. DiBardino, L. B. Yarmus, and R. W. Semaan, "Transthoracic needle biopsy of the lung." *Journal of thoracic disease*, vol. 7, no. Suppl 4, pp. S304–16, dec 2015.
- [4] J. Rosell, A. Perez, P. Cabras, and A. Rosell, "Motion planning for the Virtual Bronchoscopy," in *2012 IEEE International Conference on Robotics and Automation*. IEEE, may 2012, pp. 2932–2937.
- [5] I. Khan, R. Chin, N. Adair, A. Chatterjee, E. Haponik, and J. Conforti, "Electromagnetic Navigation Bronchoscopy in the Diagnosis of Peripheral Lung Lesions," *Clinical Pulmonary Medicine*, vol. 18, no. 1, pp. 42–45, jan 2011.
- [6] P. J. Reynisson, H. O. Leira, T. N. Hernes, E. F. Hofstad, M. Scali, H. Sorger, T. Amundsen, F. Lindseth, and T. Langø, "Navigated Bronchoscopy," *Journal of Bronchology & Interventional Pulmonology*, vol. 21, no. 3, pp. 242–264, jul 2014.
- [7] L. Rai, J. P. Helferty, and W. E. Higgins, "Combined video tracking and image-video registration for continuous bronchoscopic guidance," *International Journal of Computer Assisted Radiology and Surgery*, vol. 3, no. 3-4, pp. 315–329, sep 2008.
- [8] K. Mori, D. Deguchi, J.-i. Hasegawa, Y. Suenaga, J.-i. Toriwaki, H. Takabatake, and H. Natori, "A Method for Tracking the Camera Motion of Real Endoscope by Epipolar Geometry Analysis and Virtual Endoscopy System." Springer, Berlin, Heidelberg, oct 2001, pp. 1–8.
- [9] P. D. Byrnes and W. E. Higgins, "Construction of a multimodal CT-video chest model," Z. R. Yaniv and D. R. Holmes, Eds., vol. 9036. International Society for Optics and Photonics, mar 2014, p. 903607.
- [10] M. Visentini-Scarzanella, T. Sugiura, T. Kaneko, and S. Koto, "Deep monocular 3D reconstruction for assisted navigation in bronchoscopy," *International Journal of Computer Assisted Radiology and Surgery*, vol. 12, no. 7, pp. 1089–1099, jul 2017.
- [11] M. Shen, S. Giannarou, P. L. Shah, and G.-Z. Yang, "BRANCH:Bifurcation Recognition for Airway Navigation based on structural Characteristics." Springer, Cham, 2017, pp. 182–189.
- [12] C. Sánchez, A. Esteban-Lansaque, A. Borrás, M. Diez-Ferrer, A. Rosell, and D. Gil, "Towards a Videobronchoscopy Localization System from Airway Centre Tracking," in *VISIGRAPP (4: VISAPP)*, 2017, pp. 352–359.
- [13] E. F. Hofstad, H. Sorger, H. O. Leira, T. Amundsen, and T. Langø, "Automatic registration of CT images to patient during the initial phase of bronchoscopy: A clinical pilot study," *Medical Physics*, vol. 41, no. 4, p. 041903, mar 2014.
- [14] X. Luo and K. Mori, "A Discriminative Structural Similarity Measure and its Application to Video-Volume Registration for Endoscope Three-Dimensional Motion Tracking," *IEEE Transactions on Medical Imaging*, vol. 33, no. 6, pp. 1248–1261, jun 2014.
- [15] S. A. Merritt, R. Khare, R. Bascom, and W. E. Higgins, "Interactive CT-Video Registration for the Continuous Guidance of Bronchoscopy," *IEEE Transactions on Medical Imaging*, vol. 32, no. 8, pp. 1376–1396, aug 2013.
- [16] X. Zhou, M. Zhu, S. Leonardos, K. G. Derpanis, and K. Daniilidis, "Sparseness Meets Deepness: 3D Human Pose Estimation From Monocular Video," in *The IEEE Conference on Computer Vision and Pattern Recognition (CVPR)*, jun 2016.
- [17] OpenAI, *et al.*, "Learning Dexterous In-Hand Manipulation," aug 2018.
- [18] J. Tobin, R. Fong, A. Ray, J. Schneider, W. Zaremba, and P. Abbeel, "Domain randomization for transferring deep neural networks from simulation to the real world," in *2017 IEEE/RSJ International Conference on Intelligent Robots and Systems (IROS)*. IEEE, sep 2017, pp. 23–30.
- [19] J.-Y. Zhu, T. Park, P. Isola, and A. A. Efros, "Unpaired Image-to-Image Translation using Cycle-Consistent Adversarial Networks," mar 2017.
- [20] J. J. Craig, *Introduction to robotics: mechanics and control*. Pearson Prentice Hall Upper Saddle River, 2005, vol. 3.
- [21] K. He, X. Zhang, S. Ren, and J. Sun, "Deep Residual Learning for Image Recognition," dec 2015.
- [22] M. Abadi, *et al.*, "TensorFlow: A system for large-scale machine learning," in *12th USENIX Symposium on Operating Systems Design and Implementation (OSDI 16)*, 2016, pp. 265–283.
- [23] R. Fletcher and M. J. D. Powell, "A Rapidly Convergent Descent Method for Minimization," *The Computer Journal*, vol. 6, no. 2, pp. 163–168, aug 1963.
- [24] M. Fletcher and R. Liebscher, "PyOpenGL—the Python OpenGL binding," URL: <http://pyopengl.sourceforge.net>, 2005.
- [25] A. Mansoor, U. Bagci, B. Foster, Z. Xu, G. Z. Papadakis, L. R. Folio, J. K. Udupa, and D. J. Mollura, "Segmentation and image analysis of abnormal lungs at CT: current approaches, challenges, and future trends," *RadioGraphics*, vol. 35, no. 4, pp. 1056–1076, 2015.
- [26] W. E. Higgins, J. P. Helferty, K. Lu, S. A. Merritt, L. Rai, and K.-C. Yu, "3D CT-Video Fusion for Image-Guided Bronchoscopy," *Computerized Medical Imaging and Graphics*, vol. 32, no. 3, pp. 159–173, apr 2008.
- [27] J. Johnson, A. Alahi, and L. Fei-Fei, "Perceptual Losses for Real-Time Style Transfer and Super-Resolution," mar 2016.
- [28] R. J. Metzger, O. D. Klein, G. R. Martin, and M. A. Krasnow, "The branching programme of mouse lung development," *Nature*, vol. 453, no. 7196, pp. 745–750, jun 2008.